

<https://doi.org/10.1038/s43247-024-01266-1>

Tremor along the Dead Sea Transform remotely triggered by the 2023 M_W 7.6 Kahramanmaraş earthquake

Check for updates

Asaf Inbal ¹

Tremor signals are weak and emergent, and the physics governing their generation is not well understood. Here, I report on tremor occurring along the Dead Sea Transform (DST), and a microearthquake on the Carmel-Fari'a Fault (CFF), both remotely triggered by the 2023 M_W 7.6 Kahramanmaraş earthquake. The triggered events location coincides with maxima of long-period velocity gradients, concentrated in the CFF-DST intersection and near a CFF fault-jump. Relative to other remotely triggered tremors, the DST tremor is strong and deficient in high-frequency seismic energy. Furthermore, analysis of several remotely triggered tremor episodes suggests that tremors spectral fall-off rates are not universal. I discuss the seismological attributes that may give rise to these observations in the context of two models. In the first, tremor is produced due to inertial vibrations of a frictionally-controlled oscillator, and in the second it is produced by a swarm of Low-Frequency Earthquakes.

Tectonic tremor spectra are notoriously difficult to model. At frequencies lower than about 1 Hz the signal is masked by the ambient seismic noise, and at frequencies exceeding 1 Hz, it is obscured by the coda waves excited by multiple nearly collocated tremor sources. The resulting spectra are enriched in low-frequencies, peak between 2 to 8 Hz, and decay sharply at higher frequencies. Several models have been proposed to reproduce these observations, some are deterministic¹⁻³, and others statistical^{4,5} or stochastic^{6,7}. According to some models, tremor is composed of a sequence of low-frequency earthquakes (LFEs), such termed since they are depleted in high-frequencies relative to similar-magnitude regular earthquakes^{4,5,8}. In another model, tremor is produced due to inertial vibrations of a frictionally-controlled oscillator³. Both models reproduce the first-order temporal and spectral observations of tremor, but carry different implications with regards to the tremor source physics.

For elucidating the physics controlling tremorigenic fault behavior, it is instructive to classify tremor into one of two categories: spontaneous and instantaneous remotely triggered. The former is mostly contemporaneous with days-to-weeks-long episodic slow-slip events (SSEs), and the latter occurs only during the passage of seismic waves excited by large earthquakes. Thus, spontaneous tremors are often correlated with geodetically-detectable slow fault slip, but triggered tremors are not⁹. Despite the lack of a geodetic signal, two factors facilitate the analysis of triggered tremors relative

to their spontaneous counterpart. First, their amplitude is usually larger, and second, the transient stresses leading to remote triggering are much better constrained than the stresses promoting spontaneous tremorigenic behavior. These properties are useful for deriving and validating tremor source models.

The 2023 Kahramanmaraş earthquake pair dramatically altered the seismicity rates in Palestine and Israel¹⁰. The structure most affecting that region is the Dead Sea Transform (DST), a major plate boundary accommodating about 5 mm/yr of relative motion between the Sinai sub-plate and the Arabic plate. Large earthquakes, which rarely occur around the DST, generate long-period energy that interacts with deep geologic structures, offering the opportunity to probe seismogenic processes along the slowly-deforming DST. This study provides the first account of tremor along the DST. The tremor episode, located in the Jordan Valley section of the DST, was triggered by the M_W 7.6 Kahramanmaraş mainshock. The fault segment nearest to the tremor source is a seismic gap, which was ruptured by large $M > 7$ earthquakes in the past, but has not produced any significant earthquakes for about 1000 years¹¹. The tremor spectra are analyzed, and compared to the spectra of previously reported remotely triggered tremors. This comparison highlights differences in the tremors strength and the ground-motion spectral fall-off rates. Finally, two mathematical tremor source models that give rise to the observed variability in the spectral fall-off rates are introduced, and their mechanical implications are discussed.

¹Department of Geophysics, Tel Aviv University, Tel Aviv, Israel. e-mail: asafinbal@tauex.tau.ac.il

Results

Tremor identification and location

The 2023 destructive Kahramanmaraş earthquake doublet in south-east Turkey consisted of a $M_W7.8$ mainshock followed 9 hours later by a $M_W7.6$ mainshock. Stresses induced by these two mainshocks triggered vigorous seismic activity at remote sites located along the DST fault system, especially along the Carmel-Fari'a Fault (CFF) system¹⁰. To search for remotely triggered tremor, I scanned acceleration and velocity seismograms recorded by TRUAA, a dense network recently installed in Israel and Palestine¹². Following ref. ¹³, I filtered the acceleration time-series between 8 to 16 Hz, and visually inspected these seismograms to look for tremor-like signals arriving during the passage of the surface waves excited by the two Turkish mainshocks (see “Methods”).

Tremor-like signals were detected on several seismograms from the Jordan Valley section of the DST, north of the Dead Sea lake (Fig. 1). Figure 2a shows the ground acceleration and velocity, derived by integrating the accelerations, recorded at HMDT (location indicated in Fig. 1a). The low-pass filtered, rotated velocity time-series clearly show the surface-wave

arrivals. The top trace in panel 2a contains two high-frequency bursts aligned with the Love wave amplitude maxima, and that are apparent on all three-component band-pass filtered acceleration time-series (Fig. 2b). Similar to triggered tremor recorded elsewhere^{13–16}, the DST signals are low amplitude, emergent, correlated with maximum surface-wave energy, and do not contain any visually discernible body-wave arrivals. The duration of each tremor burst is about 10 s, close to the dominant Love wave period. I found that tremor signal only exceeded the noise level in the interval containing the strongest Love wave energy. Once the surface wave energy had decayed the tremor signal vanished.

The tremor-like signals are markedly different from signals due to regular local DST earthquakes. Figures S4–S8 present a comparison between the seismograms of the tremor-like signal to the seismograms of a regular M2.1 earthquake that occurred within about 5 km from the tremor source (see Table S1 for the earthquake’s hypocentral parameters). This comparison highlights significant differences in the temporal attributes of the two signals: the duration of detected signal is longer than the duration of a typical earthquake S-wave and its coda (e.g., vertical component at stations MEHL

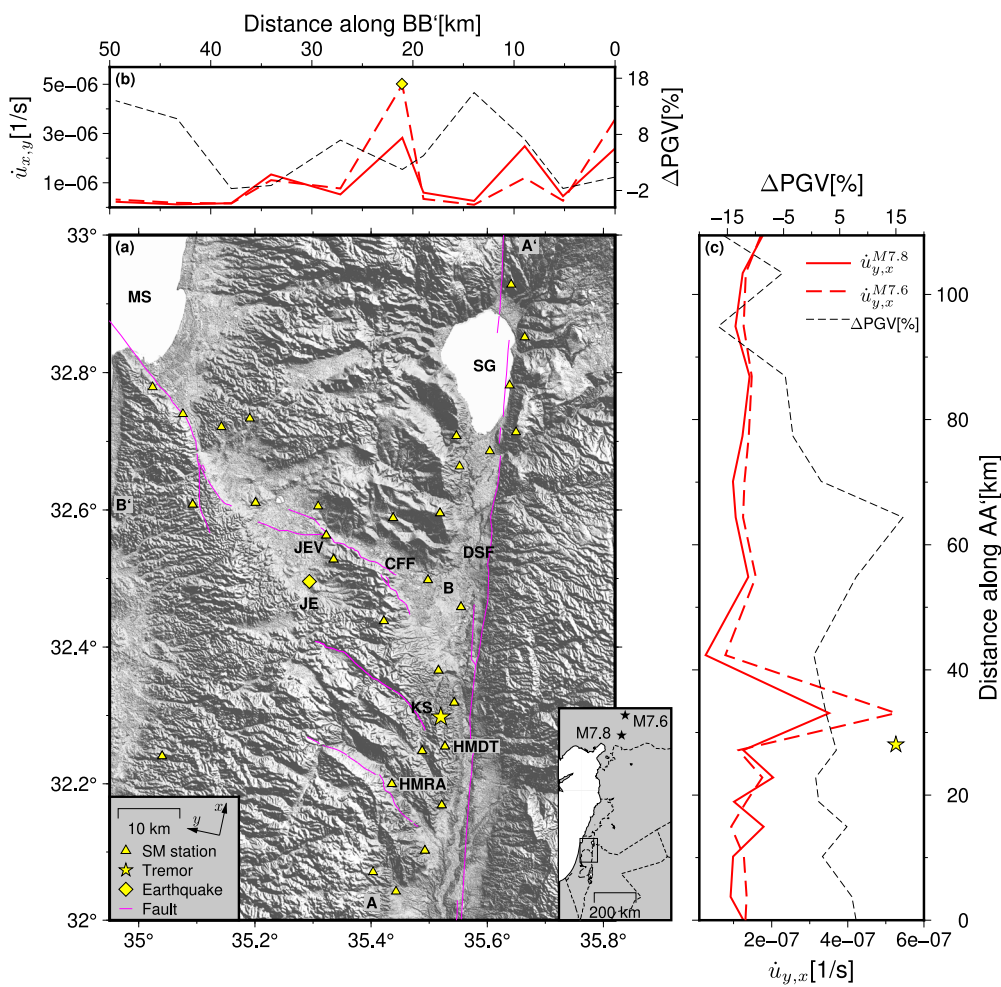


Fig. 1 | The location of triggered tremor, triggered earthquake, and strong-motion stations, and the ground-motion excited by the 2023 Turkish mainshocks in the Jordan and Jezre'el valleys. Inset map show the Eastern Mediterranean region with the the $M_{W7.8}$ and the $M_{W7.6}$ locations indicated by stars. The rectangle indicates the location of the study area, and dashed lines are for political borders. **a** Yellow triangles, star, and diamond indicate the location of the TRUAA strong-motion (SM) stations, triggered tremor, and triggered earthquake, respectively. Purple lines are for mapped faults⁵⁹. Digital elevation model provided by the Advanced Land Observing Satellite mission⁶⁰. DSF: Dead Sea Fault; CFF: Carmel-Fari'a Fault; MS: Mediterranean Sea; SG: Sea of Galilee; JE: Jenin; KS: Kirbhet Samara; JEV: Jezre'el Valley. **b**, **c** The surface-wave induced ground motions in the Jordan and Jezre'el valleys. The

difference in percent between the PGVs of the $M_{W7.6}$ and the $M_{W7.8}$ mainshocks is denoted by ΔPGV and equal to $100 \times (PGV^{M_{W7.6}} - PGV^{M_{W7.8}}) / PGV^{M_{W7.8}}$ is shown by the black dashed curve. The root-mean-square of the dynamic velocity gradients due to the $M_{W7.8}$ and the $M_{W7.6}$ are shown by the red and dashed red lines, respectively. The axes convention is shown in the legend in panel (a), with the radial and transverse directions denoted x and y , respectively. The location of the triggered tremor projected onto profile A-A' is indicated by the yellow star in panel (b), and the location of the triggered earthquake projected onto profile B-B' is indicated by the yellow diamond in panel (c). **b** The 64 to 32 s transverse ground velocity gradient, denoted by $\dot{u}_{y,x}$, as a function of position along profile A-A'. **c** The 32 to 16 s radial ground velocity gradient, denoted by $\dot{u}_{x,y}$, as a function of position along profile B-B'.

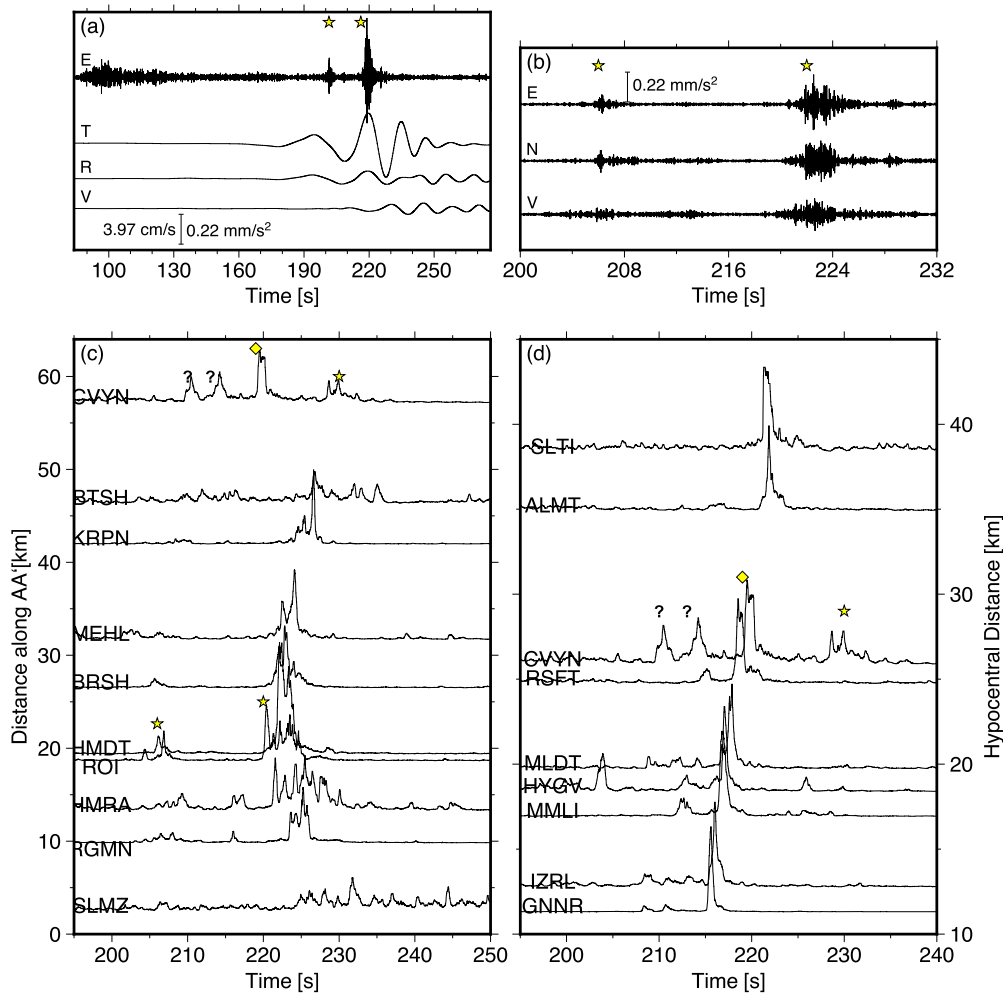


Fig. 2 | Velocity and acceleration time-series in the Jordan and Jezre'el valleys. Times are referenced to the $M_W7.6$ origin time. E, N, V, T, and R denote the east-west, north-south, vertical, transverse, and radial components, respectively. The star and diamond indicate the arrivals from the triggered tremor and the triggered earthquake, respectively. Question marks indicate unidentified arrivals. **a** Top trace is for the 8 to 16 Hz band-pass filtered acceleration time-series at HMDT, shifted to account for the source-to-station S-wave propagation time. Second, third, and fourth traces from the top are for the 0.1 Hz low-pass filtered velocities at HMDT.

b The three-component 8 to 16 Hz band-pass filtered acceleration time series at HMDT. **c** The 8 to 16 Hz band-pass filtered energy envelopes at stations located in the Jordan Valley recording the triggered tremor (location indicated by a star in Fig. 1). Vertical axis indicates distance along profile A–A' shown in Fig. 1. **d** The 8 to 16 Hz band-pass filtered energy envelopes at stations located in the Jezre'el and Jordan valleys recording the triggered earthquake (location indicated by a diamond in Fig. 1). Vertical axis indicates the hypocentral distance.

and HMDT, horizontal components at station ROI), the detected signal lacks clear P- and S-wave arrivals (e.g., horizontal components in station RGMN, HMDT, BRSH, and MEHL), and does not exhibit the ubiquitous exponential-like temporal decay associated with the coda of regular-earthquake seismograms (e.g., stations RGMN, MEHL, ROI, and BRSH). Given the short distance between the two sources, it is hard to attribute their temporal differences to the gross properties of the attenuation structure or to wave scattering effects. In addition to the difference in temporal attributes, spectral analysis points out to significant differences between the DST tremor spectra to regular DST earthquake spectra, which are further analyzed below.

For analyzing low signal-to-noise (SNR) signals such as tremor, it is often useful to inspect the signal's envelope. In this study, the envelope is computed by integrating, filtering, and squaring each accelerogram, then summing across the three components in each station, and smoothing using a running median window (see "Methods"). The amplitude of these envelopes is proportional to the signal's energy, and their SNR is improved relative to the SNR of the raw data. Figure 2c presents the tremor envelope from a set of 10 stations along the DST strand (see Fig. 1). The strongest tremor is observed on stations separated by as much as 60 km, and weaker tremor is only well-observed on stations located between 0 to 30 km along

the fault's strike. I locate the strongest tremor source (e.g., 220 s; Fig. 2b) by using Envelope Cross-Correlation (refs. ^{14,16}; see "Methods"). Although the network geometry is almost linear, the epicentral location is quite well constrained to lie within the Jordan Valley, near the Palestinian village of Kirbhet Samara (see Fig. 1 and Figure S1), between the main DST strand and the CFF. The depth of the source, which is less well constrained, lies within 10 to 20 km, roughly at the bottom edge of the seismogenic zone of that section of the DST¹⁷. The resolved depth indicates the signal was most likely excited by a tectonic source, and its temporal and spectral attributes suggest it was not excited by a regular earthquake, but more likely by a source similar to the ones frequently associated with tectonic tremors.

The search for triggered tremor also revealed an earthquake located in the southern edge of the Jezre'el Valley, which was instantaneously triggered during the passage of the $M_W7.6$ surface waves, and was not registered in the regional catalog (Figs. 1, 2d, and S2). Due to the proximity of the two triggered sources, some of the northern Jordan Valley stations show both signals (c.f. Fig. 2c, d), but in most cases the signals do not overlap, making it possible to locate the sources separately. I use the Envelope Cross-Correlation approach to locate the earthquake, and find that it occurred about 5 km north of the city of Jenin (Fig. 1a).

Interestingly, despite its larger magnitude, the $M_{W7.8}$ mainshock did not instantaneously trigger seismic activity within the study area, nor did it trigger other sites that were remotely triggered by the $M_{W7.6}$. Owing to its source properties, the $M_{W7.8}$ triggering potential is low compared to the $M_{W7.6}$ source. Much of the $M_{W7.8}$ fault is misoriented with respect to Love-wave radiation towards the DST, and its static stress drop is smaller than the one associated with the $M_{W7.6}$ ¹⁸. Consequently, the $M_{W7.8}$ is expected to excite weaker ground motions than the $M_{W7.6}$ mainshock, possibly too low to trigger seismicity at remote sites along the DST. That expectation is only partly accounted for by the observed ground motions. The $M_{W7.6}$ Peak Ground Velocities (PGVs), which are often used as a proxy for dynamic stress changes, are on average only 5% higher than the $M_{W7.8}$ PGVs in the Jordan and Jezre'el valleys (Fig. 1b, c). Moreover, the maximal relative PGV increase, which is close to 15%, does not coincide with the instantaneously triggered source locations. To better understand why instantaneous triggered events are only associated with the $M_{W7.6}$, I analyzed the dynamic velocity gradients (see “Methods”). The results, presented in Fig. 1b, c, indicate that the gradients associated with the surface waves of the $M_{W7.6}$ are locally amplified by up to a factor of 2 relative to the $M_{W7.8}$, and that the triggered events locations coincide with the along-fault long-period deformation gradient maxima. Given its smaller magnitude, the observation that the $M_{W7.6}$ locally induced stronger long-period motion is surprising. At this preliminary stage, it is unknown which source property and structural anomalies are responsible for this amplification.

Triggered tremor ground-motion spectral characteristics

In order to characterize the DST triggered tremor source I analyzed its ground-motion spectra, and compared them to the spectra of local earthquakes and tremor instantaneously triggered along the San-Andreas Fault (SAF) in Parkfield, California (CA), the San-Jacinto Fault (SJF), CA, and in the Hikurangi subduction zone in New-Zealand. Panels 3a, b and Figure S9 present the ground-displacement spectra of the DST tremor (derived from doubly-integrated accelerations), and the S-wave spectra from 10 $1.9 < M < 3$ local earthquakes (see Table S1). The earthquake spectra are typical, showing a modest decay between 3 to 8 Hz at HMR, or 3 to 10 Hz at HMDT, followed by a rapid decay above 10 Hz, which can be attributed to inelastic attenuation. They are, however, distinct from the DST tremor spectra. In the 4 to 13 Hz frequency band, the tremor spectra fall off rapidly with frequency, at a rate that is inversely proportional to frequency cubed (see “Methods” and Figure S3), whereas the earthquake spectra decay much slower. Given the proximity between the tremor and the microearthquake sources, it is unlikely that the difference in the spectral fall-off rates is the result of the gross properties of attenuation structure, but rather that it manifests a property of the tremor source or of the medium in its immediate vicinity.

The DST tremor spectral shape was compared to the spectral shapes of other triggered tremor episodes. I analyzed tremor episodes triggered along the Parkfield section of the SAF¹⁴, along the central section of the SJF^{13,16}, and in the Hikurangi subduction zone¹⁵. The results are illustrated in Fig. 3c, which presents spectra corrected for geometrical spreading and averaged over the recording stations (see “Methods”). Relative to other triggered tremors, the DST tremor is found to be strong and extremely high-frequency energy deficient. I find that the DST tremor spectra in the frequency range below 4 Hz is dominated by coda waves due to the $M_{W7.6}$, which makes determining the magnitude of the tremor source very challenging. I therefore used forward-models of tremor generation in order to roughly estimate the source properties (see Discussion).

Previous studies suggest that at frequencies higher than 1 Hz, the displacement spectra of ambient tremor decay with frequency as $f^{-1.19}$, but results shown here suggest that some triggered tremor spectra behave differently. Inspection of Fig. 3c reveals that the SAF, SJF, and Hikurangi 1 to 10 Hz tremor spectra are distinct from the DST tremor spectra. The SAF spectra exhibit decay approximately proportional to f^{-1} below 5 Hz, and approximately proportional to f^{-2} above it, and the SJF spectra decays approximately as $f^{-1.5}$ between 1.5 to 8 Hz. The Hikurangi tremor spectral

shape is similar to the SJF tremor spectral shape, yet its amplitude is much stronger. Note that the amplitude difference between the SAF and Hikurangi tremors is larger than the scatter in the recorded spectra (illustrated by the clear strips around each curve), so the inferences drawn here are likely not affected by local site amplifications. Additionally, it is unlikely that the comparison between the different spectra is biased by un-modeled inelastic effects, which are generally observed to be mild below 6 Hz^{20,21}. It is also found that none of the analyzed triggered tremor spectra are as loud and as high-frequency-depleted as the JV tremor. To further investigate the physics giving rise to the tremor far-field body-wave spectral shapes, I discuss two theoretical models that capture the prominent features of the tremor source dynamics.

Discussion

The far-field tremor source spectral models

Seismic source models are often parametrized in terms of the source body-wave spectral properties. The seismic moment rate spectra are commonly written as²²:

$$\dot{M}(f) = C \frac{M_o}{1 + \left(\frac{f}{f_c}\right)^n}, \quad (1)$$

where f is the frequency, M_o is the seismic moment, determined by the low-frequency spectral amplitude, and C is a constant which accounts for wave propagation and the source radiation pattern. The parameters f_c and n are properties of the source: n describes the rate of change in spectral amplitude with frequencies well above the source characteristic frequency, and f_c , commonly referred to as the “corner-frequency”, defines the intersection between the low- and high-frequency asymptotes.

Seismic source theory predicts the far-field body-wave displacement takes the shape of a pulse whose amplitude is proportional to the seismic source moment rate \dot{M}_o , and its duration inversely proportional to f_c . At frequencies higher than f_c , the spectra decay as f^{-n} ²³. The value of n is model-dependent, and, mathematically, it is determined by the strongest discontinuity in the far-field displacement pulse. For example, in models assuming a jump discontinuity in fault slip-rate resulting from abrupt application of stress onto the fault surface or from the termination of slip along the crack's edge, the fall-off rate decay constant n is equal to 2^{24,25}. Conversely, models in which moment accelerates gradually with time yield spectra with n equal to 3²⁶. Regular earthquake spectra are characterized by high-frequency fall-off rate constant $n = 2^{23}$, but may sometimes be fitted with $n = 3$. Tremor spectra, on the other hand, are distinct. Over the range of frequencies between 1 to 10 Hz, where regular $M < 2$ earthquake far-field displacement spectra are flat, tremor spectra are reported to decay as $f^{-1.5,8,19,27}$, and in the range above 10 Hz, tremor spectra decay as $f^{-2.21,28}$ or $f^{-3,20}$. Understanding what determines those spectral shapes is essential for elucidating the tremor source.

Source models of tremor far-field body-wave spectra

I consider two models that reproduce the observed tremor spectra: in the first, tremor is modeled as the result of inertial vibrations of a frictionally-controlled oscillator, and in the second, tremor is modeled as a swarm of LFEs with prescribed ω^2 source-time functions^{23,24}. In the first model, the spectral shape is determined by the frequency of oscillation and by the duration of moment acceleration after rupture initiation, and in the second model the spectral shape is a function of the of the LFE moment rates and recurrence intervals (see “Methods”). For discussing the source properties, it is more convenient to analyze the spectra of the far-field ground displacements rather than the ground velocities, since the former are proportional to the seismic source moment rate.

Frictionally-controlled oscillatory motion has been observed in the lab²⁹, and analyzed theoretically^{30,31} and numerically^{3,32}. From a seismological perspective, oscillatory motion will give to a distinct seismic moment rate function $\dot{M}(t)$. Because $\dot{M}(t)$ is proportional to the time-derivative of

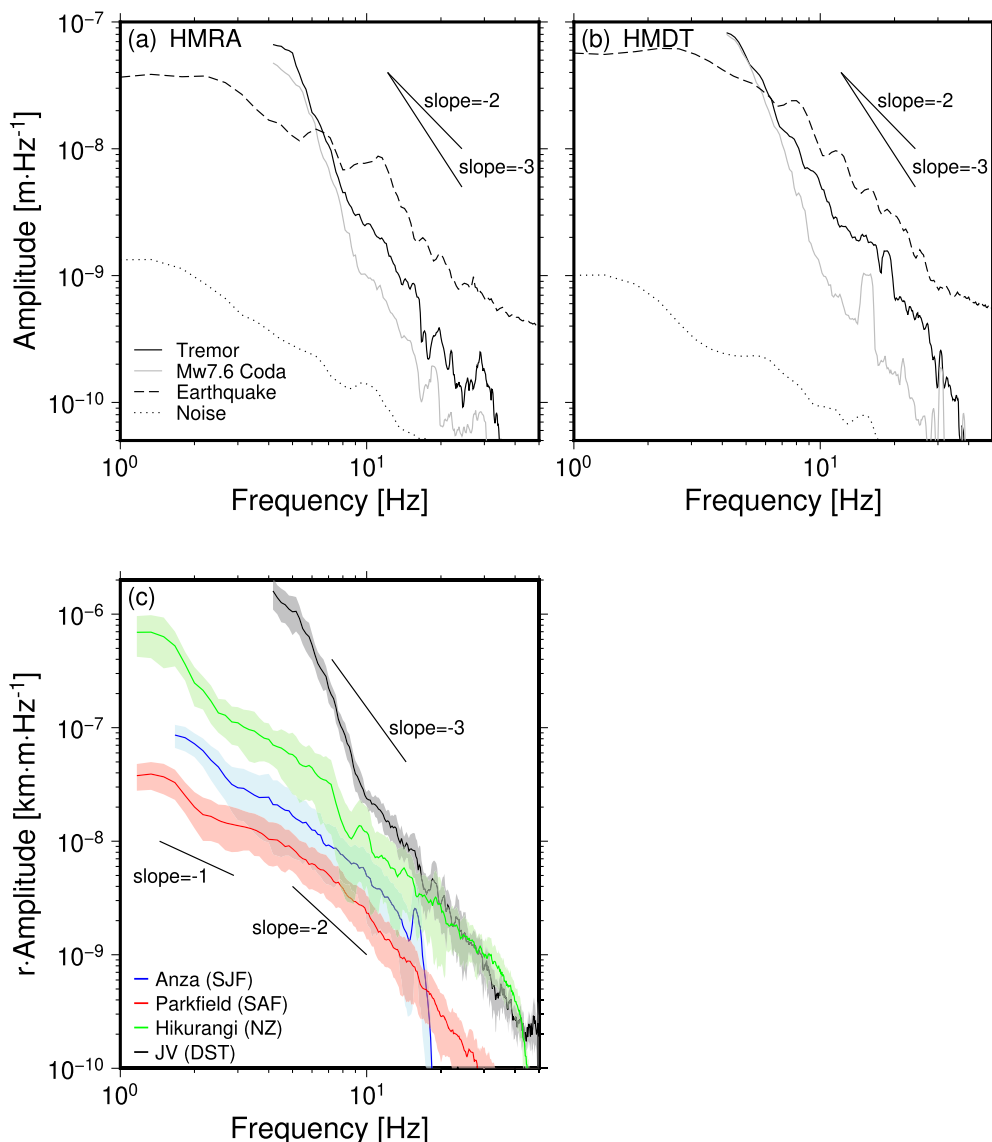


Fig. 3 | Triggered tremor and earthquake ground displacement spectra. Black, dashed black, gray, and dotted curves in panels (a) and (b) are for the Jordan Valley triggered tremor, Jordan Valley local earthquakes, the background signal in the window preceding the tremor arrivals, and the ambient noise, respectively. Panel (a) is for station HMRA and panel (b) is for station HMDT. See Fig. 1a for station locations. c The displacement spectra of triggered tremor episodes, after correcting for attenuation due to geometrical spreading along the source-to-receiver path, denoted by r . The spectra were averaged over several recording stations (see “Methods”). The light strip behind each curve indicates amplitudes within ± 1

median absolute deviation from the median. Black, green, blue, and red curves are for the Jordan Valley triggered tremor, the southern Hikurangi subduction zone, New Zealand, tremor triggered by the 2010 M_w 8.8 Maule earthquake, the Anza, Southern CA, tremor triggered by the 2002 M_w 7.8 Denali earthquake, and the Parkfield, CA, tremor triggered by the 2007 M_w 8.1 Kuril Island earthquake. To remove the surface wave signal, the Anza and Jordan Valley spectra were high-pass filtered above 1.5 and 4 Hz, respectively. SAF: San Andreas Fault; SJF: San Jacinto Fault; NZ: New Zealand; JV: Jordan Valley; DST: Dead Sea Transform.

the product between slip, δ , and area A , it is instructive to consider two variants of this model, termed here as the constant-area and the constant-slip-rate models, and shown schematically in Fig. 4a. The moment-rate functions corresponding to these models are identical. They are shown in Fig. 4b, and their spectra are shown in Fig. 4c. Note that the spectra are determined by the oscillation period τ_c and by a phase of acceleration whose duration is denoted τ_a . Spectral decay proportional to f^{-2} is obtained for a jump-discontinuity in the moment rate (blue curve in Fig. 4a), whereas spectral decay rates proportional to f^{-3} are obtained for moment-rate functions increasing linearly (blue curve) or quadratically (thin red curve) with time. The duration of the acceleration phase determines the first-order features of tremor spectra at low frequencies. When τ_a is sufficiently larger than τ_c then the spectral decay rate below $1/\tau_c$ is proportional to f^{-1} .

The mathematical LFE-swarm model was introduced by Gomberg et al.⁴, and is motivated by observations suggesting that tremor is composed of multiple nearly-collocated LFEs⁸. The spectra are computed for LFE moment-rate functions convolved with a comb function whose duration is set equal to τ_e , and that contains non-zero values whose amplitude is exponentially distributed, at intervals that are drawn from a Poissonian distribution whose scale parameter is equal to τ_s (see “Methods” and Fig. 4d). The LFE-swarm spectra can be expressed as the convolution of two functions. The first, denoted by E , modulates the LFE amplitude and the inter-LFE time intervals, denoted by τ_s . The second, denoted by S , is the LFE source time function whose duration, given by $1/f_c$, equals τ_c . Setting $n = 2$ (e.g., the ω^2 -model²⁴) and $\tau_s < \tau_c$ yields spectral amplitudes proportional to f^{-1} and f^{-2} below and above f_c , respectively (c.f. Fig. 2 in ref. ⁴). The decay rate

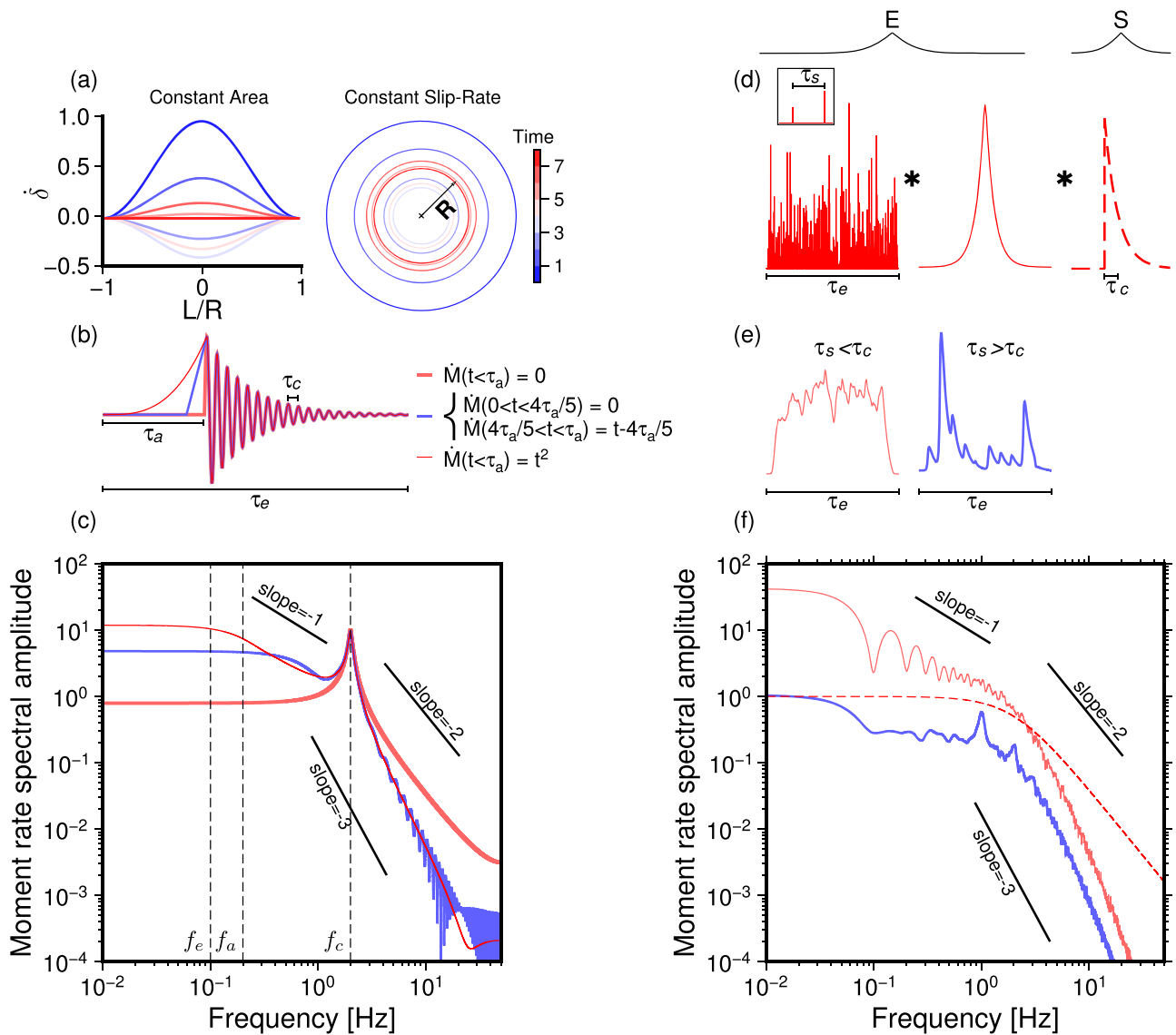


Fig. 4 | Tremor modeled moment-rate functions and resulting spectra. Left column is for the dynamic oscillator model, and right column is for the LFE-swarm model. **a** A sketch of the spatial distribution of slip. Left: Slip rate (δ) as a function of along-fault position L for the Constant Area model. Right: Location of the rupture front in the Constant Slip-Rate model. The isochrons are indicated by colors. The fault radius is denoted R . **b** The moment rate as a function of time. Thick red, blue, and light red curves are for a Heaviside, ramp, and quadratic moment rates, respectively. The duration, acceleration, and oscillation periods are given by τ_e , τ_a , and τ_c , respectively. **c** The spectral amplitude corresponding to the moment-rate functions in panel (b). The frequencies associated with the duration, acceleration, and oscillation periods are denoted f_e , f_a , and f_c , respectively. **d** A sketch of the functions constructing the LFE-swarm model. The star indicates the convolution

operator. Left: A comb function with duration given by τ_e , whose inter-spoke times follow a Poissonian distribution with a scale parameters equal to τ_s . The amplitudes of the spikes follow an exponential distribution. The inset shows a zoom-in on two adjacent spikes and the definition of τ_s . Middle: The low-pass filter response. Right: The Brune ω^2 moment-rate function with duration given by τ_c . E and S denote the functions convolved to produce the moment-rate functions in panel (e). See Section “The LFE-swarm model” for further details. **e** The LFE-swarm tremor moment-rate functions. Left: The LFE-rich model with $\tau_s < \tau_c$. Right: The LFE-poor model with $\tau_s > \tau_c$. **f** The spectral amplitude corresponding to the moment rate functions in panel (e), averaged over 20 simulations. Dashed curve is for the ω^2 moment-rate function shown in panel (d).

below f_c is determined by the number and amplitude of superposed LFE sources, which sum constructively at frequencies well-below $1/\tau_e$, and destructively at intermediate-frequencies between $1/\tau_e$ to $1/\tau_c$. The DST tremor (and also some tremor in Cascadia, (c.f., ref. ²⁰), high-frequency fall-off rates are, however, faster. The LFE-swarm high-frequency decay rate can be increased by setting n to a value larger than 2, or by smoothing E . Here I opt for the second alternative, and require E to decay as f^{-1} at frequencies above f_c . This is obtained by convolving E with a first-order zero-phase low-pass Butterworth filter, whose corner frequency is equal to $\tau_e/2$ (see “Methods”). The resulting moment-rate functions and spectra are shown in Fig. 4e, f. The light red and blue curves are for the cases $\tau_s < \tau_c$ and $\tau_s > \tau_c$,

respectively. Note that, although each LFE source time function high-frequency decay rate constant n was set equal to 2, the high-frequency portion of the spectra of the convolution $E*S$ are proportional to f^{-3} . Note also that the ratio τ_s/τ_c only affects the low-frequency portion of the spectra, which is not constrained by the Jordan Valley data set (see Fig. 3 and discussion in Section “Triggered tremor ground-motion spectral characteristics”). If $f_c \approx 5 \text{ Hz}$, then the SAF, SJF, and the Hikurangi tremor observations (Fig. 3c), suggest the portion of the spectra below f_c may be flat, or may decay as f^{-1} . In the context of the LFE-swarm model, the spectra are flattened by increasing τ_s relative to τ_c (i.e., little temporal overlap between LFE sources).

The LFE-swarm and the inertial-oscillation models are kinematically different, yet both can reproduce the DST-triggered tremor high-frequency spectra. In the LFE-swarm model, the ratio between the LFE recurrence intervals, τ_r , and the LFE durations, τ_c , controls the spectral decay rates below f_c . Low-frequency enrichment emerges due to superimposed LFE sources. Conversely, episodes enriched in high-frequencies, can be interpreted as being LFE-poor (i.e., $\tau_r > \tau_c$). The Parkfield episode (Fig. 3c) could result from LFE-poor tremor, reflecting a situation with few LFE interactions leading to diminished rates. This situation may arise if surface-wave triggering is confined to a compact area, in which the number of triggered LFE sources, and hence their interactions, are limited. Clearly, the high-frequency fall-off rate of the LFE-swarm model discussed here is tuned by filtering applied to the modulation function E . In reality, that behavior could be the result of strong near-fault attenuation, as has recently been observed in Japan³³. Like the LFE-swarm model, the inertial-oscillation model behavior is controlled by friction. However, assuming laboratory values for the constitutive parameters, sustained oscillations emerge under high loading rates or low effective stresses³. In the simple model explored here, the oscillations result in a distinct monochromatic moment-rate function, but results from 2-D simulations of³ suggest the model can also produce more realistic spectra. The low-period behavior (observed during the Parkfield and Hikurangi triggered tremors) can be compatible with observations if moment accelerates over an interval before the fault slip-rate or rupture area reach their peak. More evidence is required in order to discriminate between these two rupture modes. If slip-rate is constant, then the observations are reproduced if the rupture area oscillates. Back- and forward-propagating ruptures are frequently observed during Cascadia³⁴, Japan³⁵, and Cholame³⁶ SSEs, and thus may also characterize sources of triggered tremors.

Summary and conclusions

This is the first account of instantaneous triggering along the DST and the CFF. The triggered events epicentral locations coincide with local maxima in the $M_w7.6$ Kahramanmaraş surface-wave induced deformation rate gradients. The causes of this amplification are presently unknown. The Dead Sea Lake, bordering the study area to the south, lies within a 15 km deep sedimentary basin, however, the structure of the DST in the Jordan Valley is not well studied³⁷, and previous work does not point to structural, thermal, or gravitational anomalies that can induce such amplifications. I suspect that this local amplification is due to a structure associated with the intersection of the DST and the CFF, which could give rise to focusing of the surface wave energy or that is causing the Jordan Valley or Dead Sea Lake basins to resonant at periods of tens of seconds. Alternatively, this is the result of body-to-surface wave conversion at the basin edge, as has been reported to occur in the Kathmandu basin following the 2015 Gorkha earthquake³⁸.

I find that triggered tremor spectral shapes are variable. In frequencies between 1 to 7 Hz, the Hikurangi and SJF triggered tremor displacement spectra decay approximately as $f^{-1.5}$. Parkfield triggered tremor spectra decay as f^{-1} below 5 Hz, and as f^{-2} at higher frequencies. This, perhaps, is an additional manifestation of tremorgenic behavior of the Parkfield section, which is the only SAF section on which ambient tremor has been observed so far. The SJF, which is the most seismically active fault in southern California, sporadically produces triggered tremors^{16,39}, but whether it produces spontaneous tremors is still being debated^{40–43}. However, that fault does host triggered^{44–46} and spontaneous^{46,47} non-tremorgenic SSEs. One possibility is that the SJF becomes tremorgenic under the relatively high stressing rates associated with passing surface waves, whereas under lower loading rates the fault slips aseismically. The DST is the most high-frequency energy depleted among triggered tremors occurring on continental transform faults. It exhibits spectral fall-off rates proportional to f^{-3} . Whether the DST also produces spontaneous tremors is currently being investigated.

The tremor location indicates it is associated either with the main strand of the DST or with the CFF system. The former accommodates 4 mm/year of lateral fault motion, and is thought to be locked from the surface down to a depth of about 16 km⁴⁸. It was last ruptured by a large earthquake about 1000 years ago¹¹, and thus is considered to be a seismic gap. The latter

fault moves at about 1 mm/yr and is associated with diffused seismicity. The epicenters reported here delineate an area hosting vigorous remotely triggered seismicity following the Kahramanmaraş earthquake doublet. Collectively, these observations attest to the high level of interaction between the Kahramanmaraş faults and the DST fault system. That the DST faults were brought closer to failure underscores the importance of future seismogeodetic monitoring in that area.

Methods

Tremor identification and location via envelope cross-correlation

I restricted the analysis to data recorded by the accelerometers because the broad-band velocity seismograms across the TRUAA network were clipped during the surface wave train. I compute the envelopes by integrating to velocity, band-pass filtering between 8 to 16 Hz, squaring, summing the three components, and smoothing using a 2 s running median window.

Unlike previous reports of triggered tremor, which contain multiple visible bursts, only two of the triggered tremor bursts reported here have SNRs that are clearly above one. However, the Jordan Valley tremor is detected on accelerometers, which are not ideal for detecting weak seismic motions. Thus, the SNR levels during the coda of the $M_w7.6$ allow the detection of relatively strong bursts, while other smaller-amplitude bursts may be below the noise level. Note that curvature of the move-out of the first burst (205 s; Fig. 2b) is slightly stronger than the second burst (220 s; Fig. 2b), indicating the first source is slightly shallower than the second. I focus on the second triggered tremor burst recorded at HMDT around 220 s after the $M_w7.6$ origin time, since its SNR is higher than the first triggered tremor burst.

The cross-correlation between two envelopes is computed after shifting the traces according to a pre-computed time table. I assume a uniform S-wave velocity equal to 3 km/s and a constant depth, and compute the travel-times from a grid of possible source locations separated by 2 km in the north-south and east-west directions to each of the stations. I then shift all the traces relative to a reference stations, compute the cross-correlation, and stack. I repeat this process after varying the source depth, and associate the source location with the grid point for which the maxima of the stacked cross-correlation is maximal. Maps showing the stacked cross-correlations as a function of the tremor and earthquake source location for various source depths are presented in Figures S1 and S2, respectively.

The small number of tremor bursts associated with peak Love-wave amplitudes raises the suspicion that these signals might have been misidentified. The tremor signal is low-amplitude, and its duration and frequency content may sometime resemble the ones associated with man-made signals excited by freight trains and trucks⁴¹. The Jordan Valley is a sparsely inhabited, train-less area, and so it is unlikely that the signal is due to train or truck traffic. The area does, however, contain a number of active quarries which regularly use explosives for mining purposes, thus producing blasts that are well-recorded across the network. These blasts sometime occur around the same hours as the tremor identified here (12 am local time). However, for the reasons listed below, I consider the possibility that the signals reported here were caused by quarry blast to be unlikely. First, the detected signal coincided twice with the Love wave maximum amplitudes within 15 s. Second, the signal can be correlated among distant accelerometers located tens of km apart. Third, the signal locations are more consistent with a deep source than with a shallow source, in an area devoid of known active quarries. And forth, the spectra of registered quarry blasts differ significantly from the spectra of the signal I associate with deep tectonic tremor. In light of these observations, I conclude that the signals reported here were excited by a tectonic source. In Section “Triggered tremor ground-motion spectral characteristics” I show that the significant differences between the temporal and spectral attributes of these tremor signals to the attributes of local microearthquake seismograms also rule out the possibility that the signals I identify as tremor were actually due to an instantaneously triggered local earthquakes.

Seismograms from the nearest stations GNNR and IZRL, show two precursors to the Jezre’el Valley instantaneously triggered earthquake. These

are likely small-magnitude earthquakes also triggered by the Love waves, but they are too weak to be accurately located. The triggered earthquake signal at station CVYN was preceded by two strong precursors (indicated by the question marks in Fig. 2c, d), however, their timing and amplitude suggest they are probably not associated with the precursors recorded on GNNR, and I did not make further attempts to detect their origin.

Spectral analysis

The tremor spectra were computed for 1.5 s windows with 50% overlap encompassing 10 s of the strongest tremor, averaged over the three components. The spectra are computed using the multitaper spectral approach^{49,50}. For the DST tremor I used integrated-accelerations from the IS network starting from February 6, 2023, at 10:28:27⁵¹. For Parkfield tremor I use seismograms recorded at borehole stations from the PB and BP networks starting from January 13, 2007, at 04:49:47 UTC⁵²⁻⁵⁴. For the Anza tremor I use seismograms from the AZ network starting from November 3, 2002, at 22:34:04 UTC⁵⁵. For the Hikurangi, New-Zealand tremor I used seismograms from the NZ network starting from February 27, 2010, at 07:12:35 UTC⁵⁶.

To find the best fitting value of the spectral decay parameter n , I assume the tremor and surface wave signals are uncorrelated (i.e., their power sum constructively). I model the observed 4 to 13 Hz ground velocity power-spectral-density (PSD) as the sum:

$$|\dot{u}(f)|^2 = |Af^n|^2 + |N(f)|^2, \quad (2)$$

where A is a fitting coefficient, and $N(f)$ is the noise of the ground-velocity in the window preceding the tremor arrivals (see Fig. 3a, b). I find the value of the coefficients A and n by minimizing the differences between the right- and left-hand-side of Equation (2). The results are shown in Figure S3. The value of n best-fitting the HMRA and RGMN velocity spectra is 1.99 and 2.05, respectively. Integrating from velocity to displacement is equivalent to differentiating the spectra. Thus, the displacement spectra are approximately inversely proportional to frequency cubed for both these spectra.

Dynamic deformation gradients

The velocity gradient is computed by taking the differences between particle velocity measured at neighboring stations. Give stations i and j separated by distance measured along direction l , the k component of the velocity gradient is given by:

$$u_{k,l}^i = \frac{\dot{u}_k^j - \dot{u}_k^i}{\Delta l}, \quad (3)$$

where \dot{u}_k^i and \dot{u}_k^j are the ground velocities in direction k at station i and j , respectively. To compute the gradients along profiles A–A' and B–B' (Fig. 1b, c), I first band-pass filter, integrate the accelerations, and rotate the stations to the radial and transverse directions (shown by the arrows in the inset in Fig. 1a). I then compute the gradients between each two neighboring stations using the distance measured along the profile according to Equation (3). That results in velocity gradients time-series. For each of these time series I find the maximum amplitude, and bracket them with a window whose length is equal to 1.5 times the filter's mean period, and compute the root-mean-square (RMS) of the windowed data. The velocity gradients measurement locations are taken as the distance halfway between the two station. I apply a series of octave-band filters to the velocity gradient time-series. The filters range between 128 s to 4 s. The amplification is observed up to about 6 s. I report in Fig. 1b, c the frequency bands for which the ratio between the RMS of the $M_W7.6$ and the RMS of the $M_W7.8$ is the largest.

Mathematical models

The LFE-swarm model. The far-field spectral shape is determined by the two time-scales associated with the function modulating the LFEs, τ_s and τ_c , and by the shape of the source time function, determined by the LFE duration τ_e and the high-frequency decay constant n . The spectra can

therefore be expressed as the following convolution⁴:

$$\dot{M}(f) = E(f, \tau_s, \tau_e) \times S(f, \tau_c, n), \quad (4)$$

where the function $E(f, \tau_s, \tau_e)$ is responsible for the temporal modulation of the LFEs, and the function $S(\tau_c, n)$ is the LFE source time function. Because generally $\tau_s, \tau_c < \tau_e$, and τ_e is of the order of a few tens of seconds, the ratio $T_r = \tau_s/\tau_c$ determines the tremor source spectral behavior in the frequency band that is of interest here. In order to mimic the effect of superimposed sources, which may be thought of as a sequence of LFEs whose duration is longer than their inter-event time, I set τ_c equal to 0.5 s, and select τ_s from a random set of inter-event times that follow a Poissonian distribution with a scale parameter is equal to 0.02 s, thus producing about 300 to 500 LFEs per 10 s of tremor. For the LFE-poor model I set the mean τ_s equal to 1 s, which yields about 10 LFEs per 10 s of tremor. Setting $n = 2$, I obtained spectral decay rates equal to 1 and 2 for the frequency range $f < f_c$ and $f > f_c$, respectively. To obtain spectral decay rates proportional to f^{-3} I convolved E with a zero-phase low-pass Butterworth filter whose corner frequency is equal to 0.2 s. I run 20 iterations, compute their spectra, and report the average values in Fig. 4c.

The dynamic oscillator model

Seismic fault motion is the result of a dynamic frictional instability, which requires the frictional strength to decrease with accumulated sliding⁵⁷ or with the sliding rate^{30,58}. In addition of being slip- or velocity-weakening, to be able to nucleate earthquakes, faults must also be frictionally unstable⁵⁷. They are said to be so if their dynamic stiffness is below a critical value, which can be defined in terms of the slip-rate driving the fault^{30,31}. At low slip-rates, the critical stiffness is given by the ratio between the frictional strength drop and the slip-weakening distance. In this regime, instability is manifested as earthquake-like stick-slip events⁵⁷. At high slip-rates, however, the critical stiffness increases quadratically with the sliding-rate, and failure style is controlled by inertia^{31,32}. That theory is corroborated by lab experiments demonstrating that the response of a frictional interface changes gradually with the transition from one regime to the other³⁹, a phenomena that has come to be known as the “spectrum of slip behavior”. Numerical modeling shows that rapid stress changes imposed on weak seismic faults will cause them to resonate at particular eigenfrequencies, thereby producing tremor-like signals³. Note that, due to the strong sliding-rate dependency, any velocity weakening fault may become unstable if driven at high enough slip-rates. In this study, I simulate the tremor spectra by assuming the surface waves induced loading rate, which is of the order of mm/s to cm/s, puts the tremorgenic fault in the inertia-dominant regime. This seems to be a reasonable assumption given the long-term slip-rate on the Jordan Valley section of the DST is 5 to 6 orders of magnitude lower than the surface-wave induced rate. I set the source duration τ_e equal to 10 s, and the period of oscillation τ_c equal to 0.5 s. I damp the oscillations by multiplying with an exponential. The duration of the moment acceleration phase τ_a is 1 and 5 s for the linear and quadratic moment acceleration functions, respectively.

Data availability

Data from the IS network data recorded during the 2023 Kahramanmaraş earthquakes are available at the following <https://doi.org/10.5281/zenodo.7980346>. Other data used in this study were recorded and maintained by the following networks: the Northern California Seismic Network (<http://www.fdsn.org/datacenters/detail/NCEDC/>), the Plate Boundary Observatory Borehole Seismic Network (<http://www.fdsn.org/networks/detail/PB>), Tremorscope (<http://seismo.berkeley.edu/research/tremorscope.html>), the ANZA Seismic Network (10.7914/SN/AZ), and the New Zealand National Seismograph Network (<https://doi.org/10.21420/G19Y-9D40>).

Received: 22 June 2023; Accepted: 12 February 2024;
Published online: 28 February 2024

References

- Ben-Zion, Y. Episodic tremor and slip on a frictional interface with critical zero weakening in elastic solid. *Geophys. J. Int.* **189**, 1159–1168 (2012).
- Luo, Y. & Ampuero, J.-P. Stability of faults with heterogeneous friction properties and effective normal stress. *Tectonophysics* **733**, 257–272 (2018).
- Im, K. & Avouac, J.-P. Tectonic tremor as friction-induced inertial vibration. *Earth Planet. Sc. Lett.* **576**, 117238 (2021).
- Gomberg, J., Agnew, D. C. & Schwartz, S. Y. Alternative source models of very low frequency events. *J. Geophys. Res.* **121**, 6722–6740 (2016).
- Hawthorne, J. C. & Bartlow, N. M. Observing and modeling the spectrum of a slow slip event. *J. Geophys. Res.* **123**, 4243–4265 (2018).
- Ide, S. A Brownian walk model for slow earthquakes. *Geophys. Res. Lett.* <https://agupubs.onlinelibrary.wiley.com/doi/abs/10.1029/2008GL034821> (2008).
- Ide, S. Quantifying the time function of nonvolcanic tremor based on a stochastic model. *J. Geophys. Res.* **115**, 8313 (2010).
- Shelly, D. R., Beroza, G. C. & Ide, S. Non-volcanic tremor and low-frequency earthquake swarms. *Nature* **446**, 305–307 (2007).
- Schwartz, S. Y. & Rokosky, J. M. Slow slip events and seismic tremor at circum-Pacific subduction zones. *Rev. Geophys.* **45**, n/a–n/a (2007).
- Inbal, A., Ziv, A., Lior, I., Nof, R. N. & Eisermann, A. S. Non-triggering and then triggering of a repeating aftershock sequence in the Dead Sea by the 2023 Kahramanmaraş Earthquake pair: implications for the physics of remote delayed aftershocks. *Geophys. Res. Lett.* **50**, e2023GL104908 (2023).
- Marco, S. & Klinger, Y. *Dead Sea Transform Fault System: Reviews* (eds Garfunkel, Z., Ben-Avraham, Z. & Kagan, E.) 183–205 (Springer Netherlands, 2014).
- Kurzon, I. et al. The “TRUAA” seismic network: upgrading the Israel seismic network-toward national earthquake early warning system. *Seismo. Res. Lett.* **91**, 3236–3255 (2020).
- Gomberg, J. et al. Widespread triggering of nonvolcanic tremor in California. *Science* **319**, 173 (2008).
- Peng, Z., Vidale, J. E., Wech, A. G., Nadeau, R. M. & Creager, K. C. Remote triggering of tremor along the San Andreas Fault in central California. *J. Geophys. Res.* **114**, B00A06 (2009).
- Fry, B., Chao, K., Bannister, S., Peng, Z. & Wallace, L. Deep tremor in New Zealand triggered by the 2010 Mw8.8 Chile earthquake. *Geophys. Res. Lett.* **38**, n/a–n/a (2011).
- Wang, T.-H., Cochran, E. S., Agnew, D. & Oglesby, D. D. Infrequent triggering of tremor along the San Jacinto Fault near Anza, California. *Bull. Seismo. Soc. Am.* **103**, 2482–2497 (2013).
- Schardong, L. et al. High-quality revision of the Israeli seismic bulletin. *Seismo. Res. Lett.* **92**, 2668–2678 (2021).
- Barbot, S. et al. Slip distribution of the February 6, 2023 Mw 7.8 and Mw 7.6, Kahramanmaraş, Turkey earthquake sequence in the East Anatolian Fault Zone. *Seismica* <https://seismica.library.mcgill.ca/article/view/502> (2023).
- Ide, S., Beroza, G. C., Shelly, D. R. & Uchide, T. A scaling law for slow earthquakes. *Nature* **447**, 76–79 (2007).
- Zhang, J. et al. Cascadia tremor spectra: low corner frequencies and earthquake-like high-frequency falloff. *Geochem., Geophys., Geosyst.* **12**, n/a–n/a (2011).
- Wang, Q.-Y., Frank, W. B., Abercrombie, R. E., Obara, K. & Kato, A. What makes low-frequency earthquakes low frequency. *Sci. Adv.* **9**, eadh3688 (2023).
- Madariaga, R., Ruiz, S., Rivera, E., Leyton, F. & Baez, J. C. Near-field spectra of large earthquakes. *Pure Appl. Geophys.* 1–19 (2018).
- Aki, K. Scaling law of seismic spectrum. *J. Geophys. Res.* **72**, 1217–1231 (1967).
- Brune, J. N. Tectonic stress and the spectra of seismic shear waves from earthquakes. *J. Geophys. Res.* **75**, 4997–5009 (1970).
- Madariaga, R. Dynamics of an expanding circular fault. *Bull. Seismo. Soc. Am.* **66**, 639–666 (1976).
- Savage, J. C. Relation of corner frequency to fault dimensions. *J. Geophys. Res.* **77**, 3788–3795 (1972).
- Rubinstein, J. L. et al. Non-volcanic tremor driven by large transient shear stresses. *Nature* **448**, 579–582 (2007).
- Fletcher, J. B. & McGarr, A. Moments, magnitudes, and radiated energies of non-volcanic tremor near Cholame, CA, from ground motion spectra at UPSAR. *Geophys. Res. Lett.* **38**, n/a–n/a (2011).
- Scholz, C., Molnar, P. & Johnson, T. Detailed studies of frictional sliding of granite and implications for the earthquake mechanism. *J. Geophys. Res.* **77**, 6392–6406 (1972).
- Ruina, A. Slip instability and state variable friction laws. *J. Geophys. Res.* **88**, 10359–10370 (1983).
- Rice, J. R. & Ruina, A. L. Stability of steady frictional slipping. *J. Appl. Mech.* **50**, 343–349 (1983).
- Im, K., Marone, C. & Elsworth, D. The transition from steady frictional sliding to inertia-dominated instability with rate and state friction. *J. Mech. Phys. Solids* **122**, 116–125 (2019).
- Toh, A., Capdeville, Y., Chi, W.-C. & Ide, S. Strongly scattering medium along slow earthquake fault zones based on new observations of short-duration tremors. *Geophys. Res. Lett.* **50**, e2022GL101851 (2023).
- Houston, H., Delbridge, B. G., Wech, A. G. & Creager, K. C. Rapid tremor reversals in Cascadia generated by a weakened plate interface. *Nat. Geosci.* **4**, 404–409 (2011).
- Shelly, D. R., Beroza, G. C. & Ide, S. Complex evolution of transient slip derived from precise tremor locations in western Shikoku, Japan. *Geochem. Geophys. Geosys.* <https://agupubs.onlinelibrary.wiley.com/doi/abs/10.1029/2007GC001640> (2007).
- Inbal, A., Thomas, A. M., Newton, T. & Bürgmann, R. Complex migration of tremor near Cholame, CA, resolved by seismic array analysis. *J. Geophys. Res.* **126**, e2021JB022174 (2021).
- Garfunkel, Z. *Dead Sea Transform Fault System: Reviews* (eds Garfunkel, Z., Ben-Avraham, Z. & Kagan, E.) 183–205 (Springer Netherlands, 2014).
- Rajaure, S. et al. Characterizing the Kathmandu Valley sediment response through strong motion recordings of the 2015 Gorkha earthquake sequence. *Tectonophysics* <https://www.sciencedirect.com/science/article/pii/S004019511630395X> (2016).
- Chao, K., Peng, Z., Fabian, A. & Ojha, L. Comparisons of triggered tremor in California. *Bull. Seismo. Soc. Am.* **102**, 900–908 (2012).
- Hutchison, A. A. & Ghosh, A. Ambient tectonic tremor in the San Jacinto Fault, near the Anza Gap, detected by multiple mini seismic arrays. *Bull. Seismo. Soc. Am.* **107**, 1985–1993 (2017).
- Inbal, A. et al. Sources of long range anthropogenic noise in Southern California and Implications for Tectonic Tremor Detection. *Bull. Seismo. Soc. Am.* **108**, 3511–3527 (2018).
- Hutchison, A., Zhou, Y. & Ghosh, A. Comment on “Sources of long range anthropogenic noise in Southern California and implications for tectonic tremor detection” by A. Inbal, T. Cristea Platon, J.-P. Ampuero, G. Hillers, Duncan Agnew, and Susan E. Hough. *Bull. Seismo. Soc. Am.* <https://doi.org/10.1785/0120190171> (2023).
- Inbal, A., Cristea-Platon, T., Ampuero, J.-P., Hillers, G. & Agnew, D. Reply to Comment on “Sources of long-range anthropogenic noise in southern California and implications for tectonic tremor” by A. Hutchison, Y. Zhou, and A. Ghosh. *Bull. Seismo. Soc. Am.* <https://pubs.geoscienceworld.org/ssa/bssa/article/113/5/2232/623396/Reply-to-Comment-on-Sources-of-Long-Range> (2023).
- Inbal, A., Ampuero, J.-P. & Avouac, J.-P. Locally and remotely triggered aseismic slip on the central San Jacinto Fault near Anza, CA, from joint inversion of seismicity and strainmeter data. *J. Geophys.*

- Res. <https://agupubs.onlinelibrary.wiley.com/doi/10.1002/2016JB013499> (2017).
45. Hillers, G. et al. Seismic velocity change patterns along the San Jacinto fault zone following the 2010 M7.2 El Mayor–Cucapah and M5.4 Collins Valley earthquakes. *J. Geophys. Res.* **124**, 7171–7192 (2019).
 46. Shaddock, H. R., Schwartz, S. Y. & Bartlow, N. M. Afterslip and spontaneous aseismic slip on the Anza segment of the San Jacinto fault zone, Southern California. *J. Geophys. Res.* **126**, e2020JB020460 (2021).
 47. Sheng, Y. et al. Monitoring seismic velocity changes across the San Jacinto fault using train-generated seismic tremors. *Geophys. Res. Lett.* **49**, e2022GL098509 (2022).
 48. Sadeh, M. et al. Crustal deformation along the Dead Sea Transform and the Carmel Fault inferred from 12 years of GPS measurements. *J. Geophys. Res.* **117**, 1–14 (2012).
 49. Prieto, G., Parker, R. & Vernon, F. A fortran 90 library for multitaper spectrum analysis. *Comput. Geosci.* **35**, 1701 – 1710 (2009).
 50. Krischer, L. mtspec python wrappers 0.3.2. <https://zenodo.org/records/321789> (2016).
 51. The Israeli Seismic Network seismograms from the Mw7.8 and Mw7.5 2023 Kahramanmaras earthquakes. <https://doi.org/10.5281/zenodo.7980346> (2023).
 52. The Northern California Seismic Network. <http://www.fdsn.org/datacenters/detail/NCEDC/> (2023).
 53. The Plate Boundary Observatory Borehole Seismic Network. <http://www.fdsn.org/networks/detail/PB> (2023).
 54. The Tremorscope Seismic Network. <http://seismo.berkeley.edu/research/tremorscope.html> (2023).
 55. The ANZA Seismic Network. <https://www.fdsn.org/networks/detail/AZ/> (2023).
 56. The New Zealand National Seismograph Network. <https://nedc.nz/content/aotearoanew-zealand-geonet-seismic-digital-waveform-dataset/> (2023).
 57. Byerlee, J. D. The mechanics of stick-slip. *Tectonophysics.* **9**, 475–486 (1970).
 58. Dieterich, J. H. Modeling of rock friction 1. Experimental results and constitutive equations. *J. Geophys. Res.* **84**, 2161–2168 (1979).
 59. Sharon, M., Sagy, A., Kurzon, I., Marco, S. & Rosenshaft, M. Assessment of seismic sources and capable faults through hierarchic tectonic criteria: implications for seismic hazard in the Levant. *Nat. Hazard. Earth Syst. Sci.* **20**, 125–148 (2020).
 60. ALOS World 3D 30 meter DEM. V3.2. https://www.eorc.jaxa.jp/ALOS/en/dataset/aw3d30/aw3d30_e.htm (2021).

Acknowledgements

I wish to thank the editor Sylvain Barbot, and two anonymous reviewers for their thoughtful comments. This work benefited from discussions with A. Ziv and J.-P. Ampuero, who provided useful comments on an earlier version of the manuscript. This research was supported by ISF Grant 1802/22 and the Israeli Minister of Energy and Infrastructure Grant #72/2022.

Competing interests

The author declares no competing interests.

Additional information

Supplementary information The online version contains supplementary material available at <https://doi.org/10.1038/s43247-024-01266-1>.

Correspondence and requests for materials should be addressed to Asaf Inbal.

Peer review information *Communications Earth & Environment* thanks the anonymous reviewers for their contribution to the peer review of this work. Primary Handling Editors: Sylvain Barbot, Joe Aslin and Martina Grecequet. A peer review file is available.

Reprints and permissions information is available at <http://www.nature.com/reprints>

Publisher's note Springer Nature remains neutral with regard to jurisdictional claims in published maps and institutional affiliations.

Open Access This article is licensed under a Creative Commons Attribution 4.0 International License, which permits use, sharing, adaptation, distribution and reproduction in any medium or format, as long as you give appropriate credit to the original author(s) and the source, provide a link to the Creative Commons licence, and indicate if changes were made. The images or other third party material in this article are included in the article's Creative Commons licence, unless indicated otherwise in a credit line to the material. If material is not included in the article's Creative Commons licence and your intended use is not permitted by statutory regulation or exceeds the permitted use, you will need to obtain permission directly from the copyright holder. To view a copy of this licence, visit <http://creativecommons.org/licenses/by/4.0/>.

© The Author(s) 2024